Supplementary Information

The effects of sulfur, silicon, water, and oxygen fugacity on carbon solubility and partitioning in Fe-rich alloy and silicate melt systems at 3 GPa and 1600 °C- Implications for core-mantle differentiation and degassing of magma oceans and reduced planetary mantles

Yuan Li*, Rajdeep Dasgupta, Kyusei Tsuno (*Yuan.Li@rice.edu)

1. Analytical procedures

1.1. Electron probe microanalysis (EPMA)

Quantitative, WDS analyses of major and minor element compositions of silicate melt were carried out on a four spectrometer, Cameca SX50 electron microprobe in Texas A&M University, and the analyses of coexisting alloy melt, including carbon were on a Cameca SM-100 electron microprobe in NASA-Johnson Space Center (NASA-JSC). Determination of elemental distribution in quenched alloy melt was done using an Imix Princeton Gamma Tech (PGT) energy dispersive spectrometer (EDS) coupled to the Cameca SX50 microprobe.

For the measurement of major elements in silicate glasses, a beam diameter of 20 µm, 15 kv accelerating voltage, and 10 nA beam current for Si, Al, Fe, Mg, Ca, Na, and K and 200 nA for Ti, Cr, Mn, Ni, P, and S were used both for standardization and sample measurement. Both synthetic and natural standards were used for calibration: albite for Na, orthoclase for K, olivine for Fe, ilmenite for Ti, pyrite for S, chromite for Cr, metallic Ni for Ni, $SmPO_4$ for P, spessartine for Mn, and basaltic glass (6glbindi) for Al, Ca, Si and Mg. The peak counting time was 30 seconds expect for sulfur, which was measured for 60 seconds. Standard glasses of Indian Ocean basalt (USNM 113716) and Juan de Fuca MORB (VG-2) were routinely analyzed as secondary standards.

For analyzing the quenched alloy melt, the protocol of Dasgupta and Walker (2008) and as followed by Buono et al. (2013), Dasgupta et al. (2013a), and Chi et al. (2014) was adopted with slight modification. Carbon coat from the silicate melt analysis session was removed by re-polishing the samples. Then, the samples and standards were uncoated but surrounded with silver-bearing conductive varnish to avoid charging during EPMA analysis. The standards used included pure Ni metal, pure Fe metal, pure Si metal, natural troilite, FeS for sulfur, and synthetic Fe_3C for carbon. An anti-contaminant device cooled with liquid N_2 was used to minimize carbon blank concentration. Analytical condition for alloy melt analysis was 12 kV

accelerating voltage, 80 nA beam current, 30 micron beam diameter, and counting time of 10 s at peak and 5 s at each background.

1.2. Secondary Ionization Mass Spectrometry (SIMS)

The bulk carbon and water contents in the quenched silicate melt were determined using a Cameca IMS 1280 ion microprobe at Woods Hole Oceanographic Institution (Dasgupta et al., 2013a; Chi et al., 2014). Polished samples were mounted in indium substrate in an aluminum dish and were thoroughly cleaned with Milli-Q water and then dried in a vacuum oven at ~100 °C. Samples were then coated with ~4 nm thick gold and stored under vacuum for at least 24 hours prior to be inserted in the airlock of the instrument. A primary ion beam of $^{133}Cs^{+}$ with a current of 1-1.5 nA and with energy of 12 kV was focused to a spot of approximately 30 × 30 µm in diameter and was rastered over an area of 50 × 50 µm for 240 seconds. Negatively charged secondary ions were accelerated to energy of 10 kV into a double-focusing mass spectrometer. To reduce the potential surface contamination, ions were collected only from the central 30 x 30 µm of the beam-rastered area. Mass-analyzed ions were detected by a 22-stage Allen type electron multiplier and digitally recorded. A mass resolving power (MRP) of ~6000 was used for complete separation of $^{1}H^{16}O^{-}$ from $^{17}O^{-}$ (required MRP = 4700).

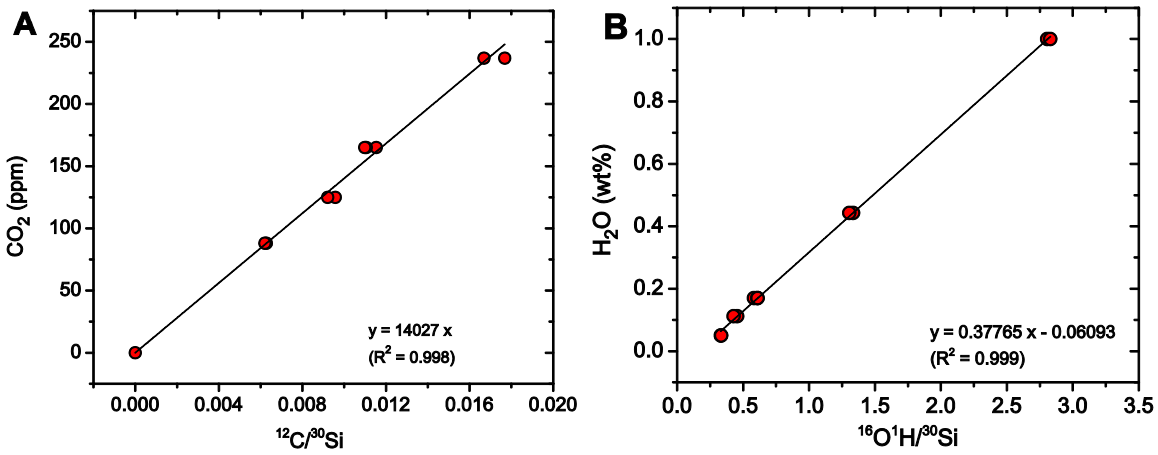

Supplementary Fig. 1. SIMS calibration for the measurement of carbon and water (H_2O) in silicate melt. See supplementary text for details.

Calibration curves shown in supplementary Fig. 1 for H_2O and CO_2 were obtained by replicate measurements of $^{12}C/^{30}Si$ and $^{1}H^{16}O/^{30}Si$ ratios in standard glasses of basaltic

composition. CO_2 and H_2O contents in the standards determined by FTIR spectroscopy and/or manometry can be found in Helo et al. (2011). About 3-6 spots were analyzed for each sample glass and each spot included 10 analytical cycles. During each cycle, a sequence of ^{12}C, $^{1}H^{16}O$ and ^{30}Si was recorded and intensity ratio of $^{12}C/^{30}Si$ and $^{1}H^{16}O/^{30}Si$ were converted to C and H (reported as H_2O) contents using the calibration curves presented in supplementary Fig. 1. Following every three analytical spots on the sample glass, one or two analyses was performed on the standard glass (ALV 519-4-1) for checking the possible deviation and thus accuracy during the analysis. It was found that during our analytical duration of ~72 hours, the CO_2 content in the standard glass (ALV 519-4-1) calculated based on the calibration curve in supplementary Fig. 1 were in good agreement with its nominal value, whereas the calculated H_2O content was about 10% lower than its nominal value (see supplementary Fig. 2).

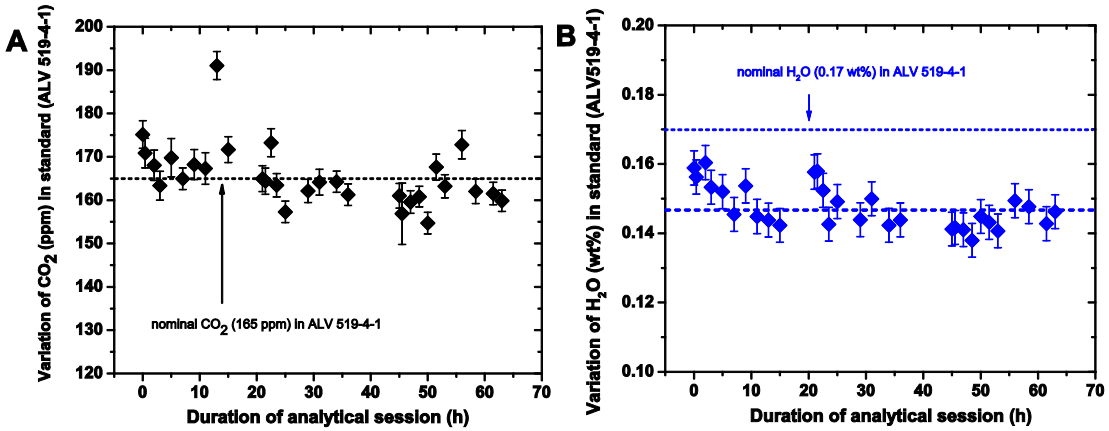

Supplementary Fig. 2. The measured CO_2 and H_2O contents in the standard glass (ALV 519-4-1) during the analytical session, based on the calibration curve presented in supplementary Fig. 1. See supplementary text for details.

1.3. Raman and Fourier-Transform Infrared Spectroscopy

A Renishaw inVia Raman microscope equipped with a 514 nm laser at Rice University was employed (Chi et al., 2014), and Raman spectra were collected in the frequency range of 200-4500 cm^{-1} with 1 cm^{-1} resolution, using a 50× objective lens and output power of 23 mW. Differing from previous studies (e.g., Stanley et al., 2014; Chi et al., 2014), spectrum at each

point in this study was accumulated 2 times with exposure time up to 400 seconds to detect the possible C-H-O species with very low contents.

FTIR spectroscopy with a Thermo Nicolet Fourier Transform Infrared Spectrometer was employed following recent protocol (Duncan and Dasgupta, 2014). Sample glasses were doubly polished to thicknesses of 200-400 μm, and immersed into acetone for 24 hours before analysis. Spectra were recorded with 4 cm^{-1} resolution, from 650 to 4000 cm^{-1}, averaging 128 scans. A nitrogen purge was used to eliminate atmospheric gases with backgrounds collected before each analysis.

2. The controls of C solubility and 'water' content on $D_C^{metal/silicate}$

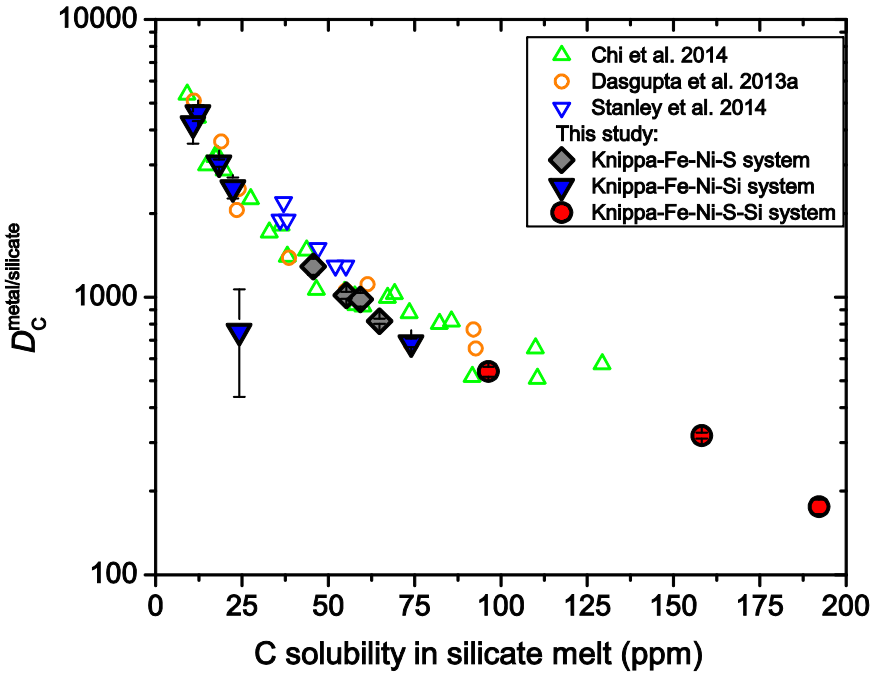

Supplementary Fig. 3. Experimental $D_C^{metal/silicate}$ values and carbon solubility at graphite saturation from this study compared to previous studies (Dasgupta et al., 2013a; Chi et al., 2014; Stanley et al., 2014). The figure shows that the $D_C^{metal/silicate}$ scales with silicate melt C content with >100 ppm C solubility in silicate melt achieved through enhanced solubility of methane at fO_2<IW-4. The figure also shows that present study performed at a single *P-T* resulted in C solubility and $D_C^{metal/silicate}$ spanning the entire range of values and beyond that were reported in previous studies over a range of *P-T*. This observation highlights the importance of melt hydration and fO_2 on these two parameters.

3. Supplementary Tables

Supplemenatry Table 1. Major element compositions of quenched silicate melts (in wt%).

Ex.ID	SiO_2	TiO_2	Al_2O_3	Cr_2O_3	FeO*	MnO	MgO	NiO	CaO	Na_2O	K_2O	P_2O_5	S	Total
G316-02	40.0	3.1	11.0	0.06	15.9	0.19	13.1	0.01	11.3	3.0	1.8	0.71	0.12	100.2
1stdv	0.4	0.2	0.1	0.01	0.3	0.00	0.1	0.01	0.1	0.1	0.0	0.17	0.00	0.5
G315-01	39.8	3.2	11.1	0.05	15.5	0.18	12.8	0.01	11.4	2.9	1.8	0.74	0.13	99.6
1stdv	0.2	0.2	0.1	0.02	0.3	0.01	0.1	0.01	0.1	0.0	0.0	0.08	0.01	0.4
G317-03	38.8	3.2	10.5	0.06	16.2	0.19	12.5	0.01	11.3	2.9	1.7	0.73	0.16	98.2
1stdv	0.3	0.2	0.1	0.01	0.3	0.01	0.1	0.01	0.1	0.1	0.0	0.17	0.01	0.7
G318-04	38.9	3.2	10.6	0.06	16.9	0.17	13.0	0.01	11.1	2.8	1.7	0.74	0.21	99.4
1stdv	0.2	0.1	0.1	0.01	0.2	0.06	0.2	0.01	0.1	0.1	0.0	0.15	0.01	0.4
G319-05	45.1	3.4	11.7	0.05	9.2	0.19	13.4	0.01	12.0	3.2	1.9	0.32	<d.l	100.4
1stdv	0.3	0.1	0.1	0.01	0.1	0.01	0.1	0.01	0.1	0.1	0.0	0.01		0.3
G320-06	46.6	3.4	11.7	0.05	6.9	0.20	13.4	0.00	12.1	3.1	1.9	0.14	<d.l	99.5
1stdv	0.2	0.2	0.1	0.01	0.2	0.01	0.1	0.00	0.1	0.1	0.0	0.01		0.4
G321-07	50.2	3.5	12.5	0.03	3.2	0.20	13.5	0.00	11.8	3.4	2.1	0.02	<d.l	100.5
1stdv	0.4	0.2	0.1	0.00	0.1	0.01	0.2	0.00	0.1	0.1	0.0	0.01		0.7
G322-08	52.4	3.5	12.8	0.01	0.36	0.19	13.7	0.00	11.9	3.3	2.2	0.00	<d.l	100.4
1stdv	0.4	0.1	0.1	0.01	0.04	0.00	0.1	0.01	0.1	0.1	0.0	0.00		0.7
G326-12	53.9	2.6	13.1	<d.l	0.17	0.09	13.0	<d.l	11.3	3.3	2.5	<d.l	<d.l	100.0
1stdv	0.3	0.1	0.3		0.11	0.01	0.2		0.2	0.1	0.1			0.5
G329-15	53.5	3.4	12.8	<d.l	0.26	0.15	14.0	<d.l	12.1	3.3	2.2	<d.l	<d.l	101.7
1stdv	0.2	0.1	0.1		0.14	0.01	0.1		0.1	0.1	0.1			0.5
G330-16	53.6	3.3	11.6	<d.l	0.29	0.16	13.5	<d.l	12.2	3.1	1.9	<d.l	0.69	100.4
1stdv	0.2	0.2	0.1		0.04	0.01	0.1		0.1	0.1	0.0		0.01	0.3
G331-17	53.6	3.1	11.4	<d.l	0.20	0.14	13.2	<d.l	12.1	3.0	1.9	<d.l	1.06	99.7
1stdv	0.3	0.1	0.1		0.04	0.01	0.1		0.1	0.1	0.0		0.01	0.5
G337-19	54.3	2.9	11.9	<d.l	0.18	0.12	13.6	<d.l	11.8	3.1	1.9	<d.l	2.57	102.3
1stdv	0.3	0.1	0.1		0.06	0.0	0.1		0.1	0.1	0.0		0.0	0.6

Ten spots were analyzed for each sample. * FeO represents total iron oxides in silicate melt.

Supplementary Table 2. Major element composition of quenched metallic alloy melt (in wt%).

Ex.ID	Fe	Ni	Si	C	S	Total
G316-02	85.24	5.59	<d.l	5.61	2.99	99.44
1stdv	0.77	0.20		0.10	0.22	0.75
G315-01	83.81	6.64	<d.l	5.88	4.93	101.27
1stdv	0.39	0.34		0.39	0.49	0.45
G317-03	82.81	7.03	<d.l	5.81	4.43	100.10
1stdv	1.02	0.56		0.25	0.41	1.00
G318-04	86.22	5.45	<d.l	5.31	3.44	100.43
1stdv	0.53	0.19		0.08	0.45	0.52
G319-05	87.13	5.35	0.01	5.53	<d.l	98.03
1stdv	0.55	0.14	0.01	0.15		0.57
G320-06	86.97	5.01	0.01	5.58	<d.l	97.57
1stdv	0.66	0.07	0.00	0.15		0.68
G321-07	86.99	4.88	0.01	5.66	<d.l	97.55
1stdv	0.52	0.08	0.00	0.12		0.55
G322-08	87.41	4.44	0.52	5.07	<d.l	97.44
1stdv	0.38	0.06	0.01	0.17		0.80
G326-12	82.37	5.13	9.87	1.82	<d.l	99.20
1stdv	0.33	0.10	0.32	0.75		1.37
G329-15	87.48	5.11	5.16	4.54	<d.l	102.30
1stdv	0.50	0.10	0.11	0.19		0.56
G330-16	85.35	5.26	1.00	5.2	2.21	99.01
1stdv	0.53	0.18	0.04	0.09	0.82	0.60
G331-17	80.31	4.66	3.17	5.02	1.91	95.06
1stdv	0.99	0.17	0.19	0.11	1.17	0.85
G337-19	83.26	5.35	6.64	3.38	1.12	99.75
1stdv	1.78	0.11	0.49	0.20	0.33	1.49

Ten to fifteen spots were analyzed for each sample.

4. Supplementary References

Buono, A. S., Dasgupta, R., Lee, C. T.-A., and Walker, D., 2013. Siderophile element partitioning between cohenite and liquid in Fe-Ni-S-C system and implications for geochemistry of planetary cores and mantles. Geochim. Cosmochim. Acta 120, 239-250.

Chi, H., Dasgupta, R., Duncan, M., Shimizu, N., 2014. Partitioning of carbon between Fe-rich alloy melt and silicate melt in a magma ocean-Implications for the abundance and origin of volatiles in Earth, Mars, and the Moon. Geochim. Cosmochim. Acta 139, 447-471.

Dasgupta, R. and Walker, D., 2008. Carbon solubility in core melts in a shallow magma ocean environment and distribution of carbon between the Earth's core and the mantle. *Geochim. Cosmochim. Acta* 72, 4627–4641.

Dasgupta, R., Chi, H., Shimizu, N., Buono, A., and Walker, D., 2013a. Carbon solution and partitioning between metallic and silicate melts in a shallow magma ocean: implications for the origin and distribution of terrestrial carbon. *Geochim. Cosmochim. Acta* 102, 191-212.

Duncan, M.S., Dasgupta, R., 2014. CO_2 solubility and speciation in rhyolitic sediment partial melts at 1.5–3.0 GPa – Implications for carbon flux in subduction zones. Geochim. Cosmochim. Acta 124, 328-347.

Helo, C., Longpre, M.-A., Shimizu, N., Clague, D. A., Stix, J., 2011. Explosive eruptions at mid-ocean ridges driven by CO_2-rich magmas. Nat. Geosci. 4, 260-263.

Stanley, B. D., Hirschmann, M. M., and Withers, A. C., 2014. Solubility of C-O-H volatiles in graphite-saturated martian basalts. Geochim. Cosmochim. Acta 129, 54-76.